J. Fluid Mech. (2009), *vol.* 628, *pp.* 23–41.
doi:10.1017/S0022112009006090 Printed in the United Kingdom

Reversal of the lift force on an oblate bubble in a weakly viscous linear shear flow

RICHARD ADOUA[1,2], DOMINIQUE LEGENDRE[1,2] AND JACQUES MAGNAUDET[1,2]†

[1]Université de Toulouse; INPT, UPS; IMFT (Institut de Mécanique des Fluides de Toulouse); Allée Camille Soula, F-31400 Toulouse, France

[2]CNRS; IMFT; F-31400 Toulouse, France

(Received 17 October 2008 and in revised form 14 January 2009)

We compute the flow about an oblate spheroidal bubble of prescribed shape set fixed in a viscous linear shear flow in the range of moderate to high Reynolds numbers. In contrast to predictions based on inviscid theory, the numerical results reveal that for weak enough shear rates, the lift force and torque change sign in an intermediate range of Reynolds numbers when the bubble oblateness exceeds a critical value that depends on the relative shear rate. This effect is found to be due to the vorticity generated at the bubble surface which, combined with the velocity gradient associated with the upstream shear, results in a system of two counter-rotating streamwise vortices whose sign is opposite to that induced by the classical inviscid tilting of the upstream vorticity around the bubble. We show that this lift reversal mechanism is closely related to the wake instability mechanism experienced by a spheroidal bubble rising in a stagnant liquid.

1. Introduction

Bubble distribution and associated modifications of the microstructure in gravity-driven bubbly flows are of great importance in many geophysical and industrial processes. In a large number of cases, a crucial ingredient in the evolution of this distribution is the lateral or lift force acting on bubbles rising in shear flows. For instance, depending on the direction along which bubbles preferentially migrate and accumulate in wall-bounded shear flows, wall transfers (i.e. friction and heat or mass flux) can be strongly affected (Serizawa, Kataoka & Michiyoshi 1975). Thanks to various detailed experimental and computational studies, the inertial migration of nearly spherical bubbles in such flows is now fairly well understood (e.g. experiments by van Nierop *et al.* 2007 and computations by Legendre & Magnaudet 1998). The situation is much less satisfactory with larger bubbles whose shape strongly departs from sphericity. Indeed, it has been repeatedly reported in the literature, both from experiments (Kariyasaki 1987; Tomiyama *et al.* 2002) and computations (Ervin & Tryggvason 1997; Sankaranarayanan & Sundaresan 2002), that the direction of migration of such bubbles in a given shear flow reverses when their size, and hence their deformation, exceeds some critical value. Similar findings were recently reported in turbulent bubbly boundary layers (Tran-Cong, Marié & Perkins 2008), although in this case large-scale turbulent structures and near-wall effects may be

† Email address for correspondence: jacques.magnaudet@imft.fr

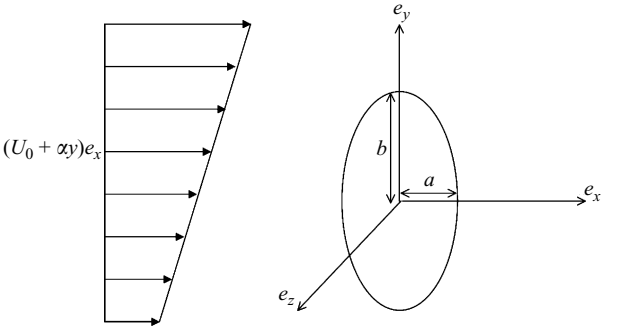

FIGURE 1. Sketch of the flow configuration.

partly responsible for the observed behaviour. This intriguing reversal migration phenomenon is at odds with predictions provided by inviscid theory, according to which, in a given shear flow, the lift force on an oblate spheroidal bubble has the same sign as that experienced by a spherical bubble (Naciri 1992). In this approximation, the generation of the lift force entirely grounds on the distortion of the upstream vorticity around the bubble. Nevertheless, this view completely neglects the existence and effect of the vorticity produced right at the bubble surface by the shear-free condition. As it is now recognized that this surface vorticity is at the root of the generation of the transverse force that leads to zigzag and helical paths of high-Reynolds-number bubbles rising in still liquid (Mougin & Magnaudet 2002; Magnaudet & Mougin 2007), it is important to understand how it interacts with the upstream vorticity and whether this interaction is capable of producing the observed lift reversal. This is the purpose of the present paper in which the above problem is studied by means of direct numerical simulation (DNS).

2. Statement of the problem

We consider an oblate spheroidal bubble with a prescribed shape characterized by the lengths b and a of the major and minor semi-axis, respectively. The bubble is maintained fixed in a linear shear flow whose upstream velocity in the Cartesian frame of reference centred at the bubble centroid is (figure 1),

$$\boldsymbol{U}_\infty = (U_0 + \alpha y)\boldsymbol{e}_x. \tag{2.1}$$

Since the gas that fills the bubble has a negligible viscosity and the gas–liquid interface is assumed to be free of any surfactants, the liquid obeys a zero shear condition at the bubble surface.

The problem is described by three dimensionless numbers, namely the Reynolds number $Re = 2bU_0/\nu$, the dimensionless shear rate $Sr = 2\alpha b/U_0$ and the bubble aspect ratio $\chi = b/a$, where ν is the kinematic viscosity of the surrounding liquid. In what follows, we explore the bubble response over a wide range of these three parameters, i.e. $Re \in [50, 4000]$, $Sr \in [0, 0.2]$, $\chi \in [1.0, 2.7]$. Note that the so-called equivalent radius of the bubble is $R_{eq} = (ab^2)^{1/3} = b\chi^{-1/3}$. Therefore, with the above definition of Re and Sr, when any of them is kept fixed for increasing χ, the bubble volume $V = 4/3\pi R_{eq}^3$ is decreasing as χ^{-1}.

The total force $\boldsymbol{F}$ acting on the bubble is decomposed into drag and lift components, the latter of which is defined as $F_L = \boldsymbol{F}_0\boldsymbol{e}_y = \frac{4}{3}C_L\pi ab^2\rho\alpha U_0$, where ρ is the liquid density and C_L is the lift coefficient. This definition stems from the fact that in the

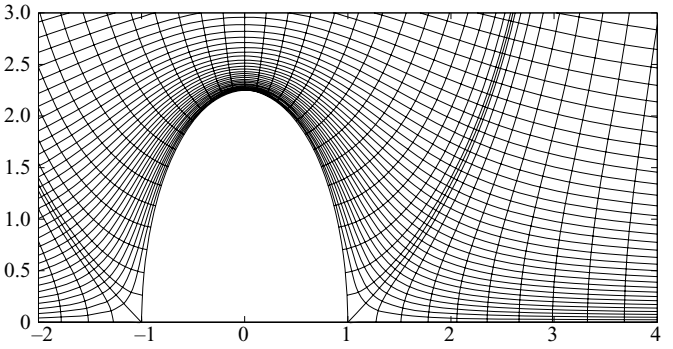

FIGURE 2. Detail of the grid ($\chi = 2.25$).

inviscid approximation and in the weak shear limit $Sr \ll 1$, an axisymmetric body of volume V whose axis is aligned with the upstream flow experiences a lift force proportional to $\rho V \alpha U_0$ (see Auton 1987 and Auton, Hunt & Prud'homme 1988 for more insight into the origin of this definition). Owing to the shear orientation, the torque $\boldsymbol{\Gamma}$ experienced by the bubble is oriented along the $\boldsymbol{e}_z$ direction and is expressed in the form $\boldsymbol{\Gamma}_0 \boldsymbol{e}_z = \frac{1}{2} C_T \pi b^4 \rho \alpha U_o$, where C_Γ is the torque coefficient. All numerical results discussed later are presented using the above dimensionless coefficients.

Of course the assumption that the bubble shape may be reasonably well approximated as an oblate spheroid puts some restriction on the parameter range in which the present study is relevant. Bubbles rising in a low-viscosity liquid at rest at infinity are known to adopt approximately oblate spheroidal shapes when their rise Reynolds number is typically in the range $O(10^2 - 10^3)$ while their Weber number $We = \rho U_0^2 b/\sigma$ is of $O(1)$, σ denoting surface tension. In presence of shear, this approximation remains relevant only in situations where the Weber number based on the inertia effect resulting from the coupling of slip and shear, i.e. $WeSr$, and that based on nonlinear shear effects, i.e. $WeSr^2$, are both much smaller than unity. To ensure that both conditions are satisfied, we assume in what follows that $We = O(1)$ and $Sr \ll 1$; this is why the largest shear rate we consider in most of the paper is $Sr = 0.2$.

3. Numerical tool and validation

The computations reported below were carried out with the JADIM code thoroughly described in several of our previous publications. In particular, we used this code to compute the lift force acting on a spherical bubble moving in a viscous linear shear flow (Legendre & Magnaudet 1998), and to analyse the physical processes governing the wake instability of a fixed spheroidal bubble (Magnaudet & Mougin 2007). Basically, the momentum equations are written in velocity–pressure variables in a general system of orthogonal curvilinear coordinates. The discretization makes use of a staggered grid on which the equations are integrated in space using a finite volume method with second-order accuracy. Advection and viscous terms are evaluated through second-order centred schemes, whereas time advancement is achieved through a second-order time accurate Runge–Kutta/Crank–Nicolson algorithm. Finally, incompressibility is satisfied at the end of each time step by solving a Poisson equation for an auxiliary potential.

A detail of the grid used in the present work is presented in figure 2 for the case of a bubble with an aspect ratio $\chi = 2.25$. The three-dimensional orthogonal grid is

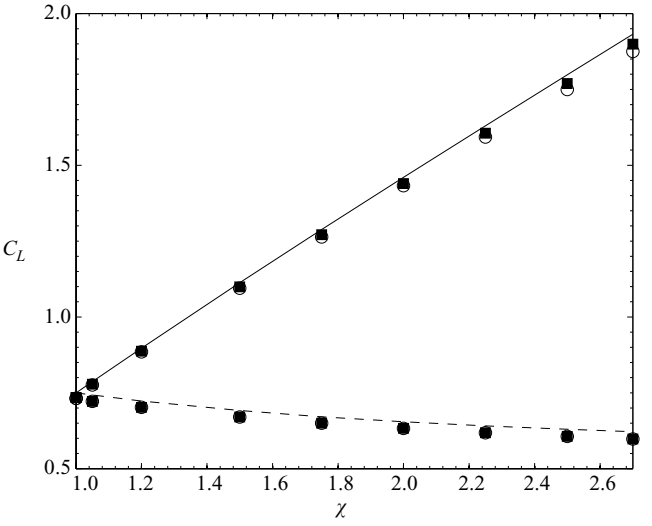

FIGURE 3. Evolution of the initial lift coefficient $C_L(t=0^+)$ with χ for $Re=1000$. Solid line: Miloh's (2003) prediction for $\boldsymbol{U}=(U_0+\alpha y)\boldsymbol{e}_x$; dashed line: Miloh's (2003) prediction for $\boldsymbol{U}=(U_0+\alpha x)\boldsymbol{e}_y$; numerical results for both configurations: ○ $Sr=0.02$, ■ $Sr=0.2$. Note that in the case of a sphere ($\chi=1$), the initial value of C_L is 0.75 (Legendre & Magnaudet 1998).

generated by rotating a two-dimensional grid about the $\boldsymbol{e}_x$-axis with an angle ϕ. The two-dimensional grid is obtained by inverting the equations defining the streamlines $\psi=const.$ and the equipotential lines $\eta=const.$ of the potential flow generated by a uniform stream around an oblate ellipsoidal cylinder. The grid employs N_b points to describe half a meridian on the bubble surface, N_x points from one bubble pole to the corresponding outer boundary along the $\boldsymbol{e}_x$-axis, N_y points along the $\boldsymbol{e}_y$-axis and N_ϕ points in the azimuthal direction ϕ. The influence of these various numbers was carefully checked to make sure that the results presented below are grid-independent (see Adoua 2007 for more details). The outer boundary of the numerical domain is a cylinder of radius R_∞ and length $2(R_\infty+a)$ (a is the minor semi-axis of the bubble). The distance R_∞ was chosen to avoid confinement effects in the wake region. To properly capture the vorticity generated at the bubble surface, four rows of cells were placed within the boundary layer whose thickness is $O(bRe^{-1/2})$ at the bubble equator. The influence of the thickness δ of the cells closest to the bubble surface was also examined in detail. Finally, the computations were performed with $N_b=30$, $N_x=50$, $N_y=70$, $N_\phi=64$, $\delta=0.003a$ and $R_\infty=50a$. In order to provide an extra validation of the code in a situation relevant to the present problem, an additional test was performed. This test consists in calculating the initial value of the lift force on a spheroidal bubble suddenly inserted in an already established linear shear flow, i.e. the value of C_L at time t such that $tU_0/b \ll 1$. The theoretical solution to this problem was recently derived by Miloh (2003) for a weak inviscid shear flow ($Sr \ll 1$). We considered two different geometrical situations, namely that studied in the rest of this paper where the upstream flow is along the bubble minor axis, and that where it is along one of the major axes. The first of these is obtained by setting $\boldsymbol{U}_\infty=(U_0+\alpha y)\boldsymbol{e}_x$, while the second corresponds to $\boldsymbol{U}_\infty=(U_0+\alpha x)\boldsymbol{e}_y$ and produces a lift force in the x-direction. Both situations were computed over the range $\chi\in[1.0, 2.7]$ for two dimensionless shear rates, namely $Sr=0.02$ and $Sr=0.2$. As observed in figure 3,

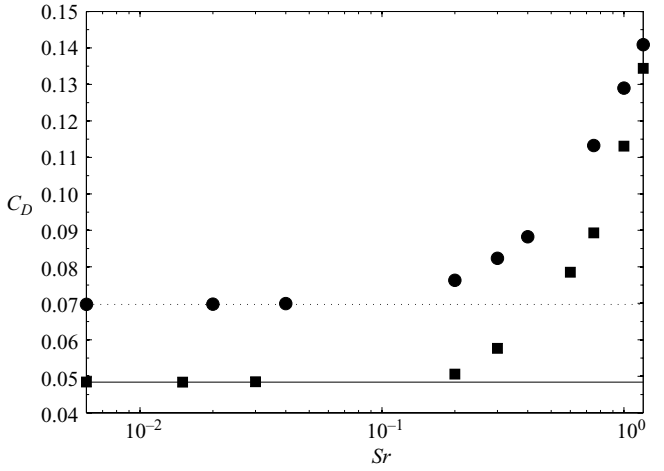

FIGURE 4. Evolution of the drag coefficient C_D with the dimensionless shear rate Sr for $Re = 1500$. ■: $\chi = 1.5$; ●: $\chi = 2.0$.

the numerical results corresponding to $Re = 1000$ are in close agreement with the theoretical prediction for both configurations.

4. Numerical results

We now turn to the computational results obtained in the range of moderate to large Reynolds numbers. We shall essentially focus on the lift force which is the most revealing global dynamic quantity in the present system. We shall also briefly comment on the hydrodynamic torque experienced by the bubble, as it is also a direct consequence of the non-zero shear. In contrast we shall not discuss the evolution of the drag force F_D in detail because this component does not reveal any unexpected trends. Here it is sufficient to say that for $Sr \leqslant 0.2$, the shear has a negligible effect on the drag force and the latter follows Moore's prediction (Moore 1965) for large enough Reynolds numbers (typically for $Re > 600$ when $\chi = 2.5$). We also performed some runs with higher shear rates. These runs revealed a discernible increase of F_D with the shear and, for large enough Re, we found the ratio $F_D(Re, Sr)/F_D(Re, Sr = 0)$ to be proportional to $1+\beta(\chi)Sr^2$. An example of this behaviour is shown in figure 4. The corresponding values of β are approximately 1.34 for $\chi = 1.5$ and 0.85 for $\chi = 2.0$. Combined with the result $\beta(\chi = 1) \approx 0.55$ obtained by Legendre & Magnaudet (1998) for a spherical bubble, these findings suggest that β evolves non-monotonously with the aspect ratio and reveal a particular sensitivity of the drag force to the shear for $\chi \approx 1.5$.

4.1. *Lift force*

Figure 5 shows the evolution of the lift coefficient as a function of the aspect ratio for four values of the Reynolds number. The numerical results are compared with the theoretical solution $C_L = C_{L\infty}(\chi)$ obtained for a weak inviscid shear flow by Naciri (1992). This solution was derived by numerically inverting a Laplace equation to determine the velocity disturbance induced by the distortion of the upstream vorticity around the body. Naciri (1992) showed that the values of $C_{L\infty}(\chi)$ very closely follow those of the added (or virtual) mass coefficient, thus extending a result already known for a spherical body (Auton 1987) (see also Wells 1996 for the connection between

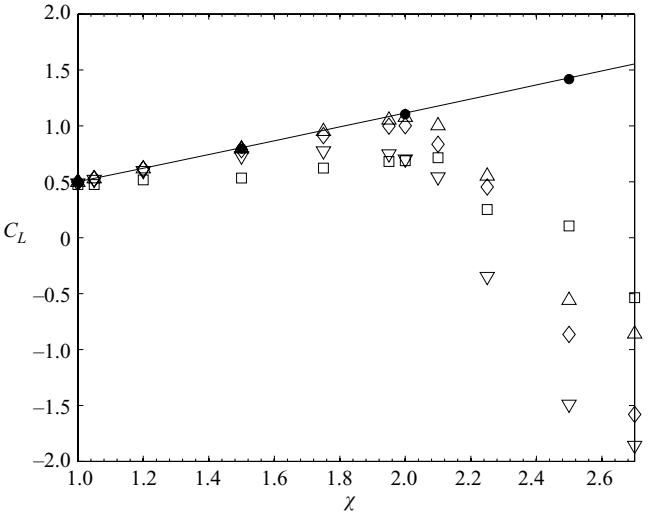

FIGURE 5. Lift coefficient C_L versus the aspect ratio χ for $Sr = 0.02$ and □ $Re = 100$; ▽ $Re = 400$; ◇ $Re = 1000$; △ $Re = 1500$; ● Naciri (1992); — relation (4.1).

added mass and inviscid lift). A simple correlation fitting Naciri's results with an accuracy better than 1 % is

$$C_{L\infty}(\chi) = 0.5 + 0.612(\chi - 1). \tag{4.1}$$

Figure 5 shows the existence of two markedly different regimes. For moderate aspect ratios ($\chi \leqslant 2.0$, approximately), the lift coefficient follows the behaviour predicted by the inviscid solution. It increases gently with the aspect ratio and tends towards $C_{L\infty}$ when the Reynolds number is large enough. A detailed examination of the difference $C_L(\chi, Re) - C_{L\infty}(\chi)$ reveals that throughout the range of parameters explored here, the evolution of C_L can be closely fitted by the simple correlation

$$C_L(\chi, Re) = C_{L\infty}(\chi) - 0.16\chi^{5/2}/\left(1 + 0.0027Re^{3/2}\right). \tag{4.2}$$

The above Re-dependent correction comes from the pressure contribution to the lift force, which is by far dominant in the regime considered here. There is also a small contribution provided by the normal viscous stress which behaves as Re^{-1}. This contribution should eventually dominate over that proportional to $Re^{-3/2}$ as Re goes to infinity. However, the prefactor of the $Re^{-3/2}$ term is much larger, making this term dominate the overall behaviour of the difference $C_{L\infty} - C_L$ throughout the whole range of Reynolds numbers covered by present computations.

For larger oblatenesses ($\chi \geqslant 2.0$), the behaviour of the lift force changes dramatically. The lift coefficient is found to decrease strongly when χ further increases and then depends significantly on the Reynolds number. It even changes sign for certain sets of parameters, indicating that a freely rising bubble with a sufficient oblateness may migrate in the direction opposite to that followed by a spherical bubble. Within the region where C_L is found to be negative, there is a subregion within which the lift force exhibits periodic oscillations but keeps negative values all the time (see below). In such cases, the values reported in figure 5 were obtained by time-averaging the instantaneous lift coefficient. Note that the evolution of C_L with the Reynolds number is not monotonic. Among the four values of Re considered in

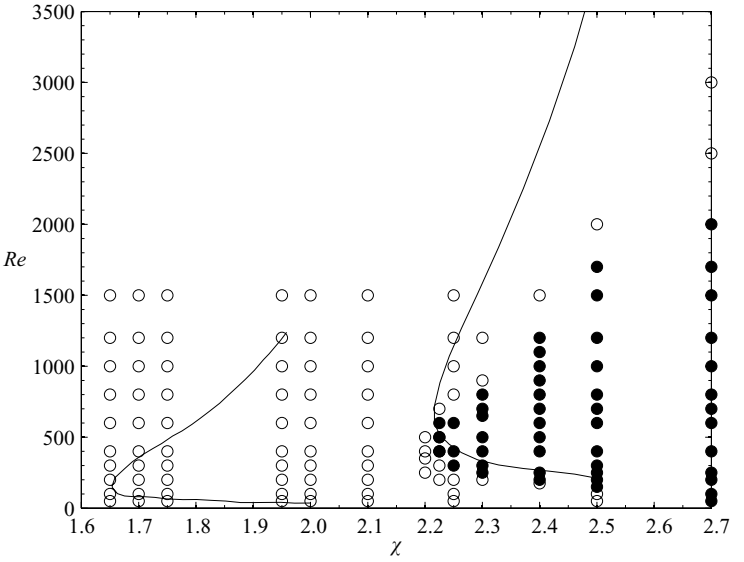

FIGURE 6. Phase diagram (χ, Re) showing the sign of the lift force for $Sr = 0.02$. ○ $C_L > 0$; ● $C_L < 0$. The solid line indicates the frontier of the domain where Magnaudet & Mougin (2007) found the axisymmetric wake of a bubble moving in a uniform flow to be unstable (their investigation was limited to $\chi \leqslant 2.5$).

figure 5, the decrease of C_L with χ reaches a maximum for $Re = 400$, while bubbles with both lower and higher Reynolds number are less affected.

Qualitatively similar evolutions were observed with several other values of Sr and Re as well. Figure 6 summarizes these results in a phase diagram showing the sign of C_L in the (χ, Re) plane in the case of a low dimensionless shear rate, namely $Sr = 0.02$. This diagram confirms that for $\chi < \chi_0(0.02) \approx 2.2$, the lift force is always positive whatever be the Reynolds number. When the aspect ratio increases beyond χ_0, there is a finite range of Reynolds number, say $[Re_1(\chi, 0.02), Re_2(\chi, 0.02)]$, within which the lift force is negative. The lower critical Reynolds number, Re_1, progressively decreases as $\chi - \chi_0$ increases, becoming of $O(10^2)$ for $\chi = 2.7$, while Re_2 increases much more rapidly with $\chi - \chi_0$ and is about 2000 for the same χ. One can wonder what happens when the Reynolds number is well beyond the upper critical value $Re_2(\chi, Sr)$. The answer is provided by figure 7 which shows how C_L evolves with χ for $Re = 4000$, a Reynolds number for which the boundary layer is still properly resolved in the computations. The comparison with the inviscid prediction indicates that, similarly to what we found for $\chi < \chi_0(Sr)$, C_L tends towards the asymptotic value computed by Naciri (1992) throughout the whole range of aspect ratios we considered. In passing, we note in figure 7 that C_L closely follows the evolution of the added mass coefficient C_M corresponding to a linear acceleration of the bubble about its symmetry axis, namely $C_M(\chi) = \alpha_0/(2-\alpha_0)$, with $\alpha_0 = 2(1+e^2)(1-e\,\cot^{-1}e)$ and $e = (1-\chi^2)^{-1/2}$ (Lamb 1945, p. 153). This numerical result confirms the equality $C_L(\chi) = C_M(\chi)$ already established by Auton (1987) (for a sphere) and Naciri (1992) (for an oblate spheroid) in the limit $Sr \to 0$, $Re \to \infty$, and indicates that this equality still holds for non-vanishing shear rates, at least up to $Sr = O(10^{-1})$.

As soon as the aspect ratio exceeds the critical value $\chi_0(Sr)$ and the Reynolds number is in the range $[Re_1(\chi, Sr), Re_2(\chi, Sr)]$, the lift force strongly depends on the dimensionless shear rate, a behaviour at odds with that observed in the left part

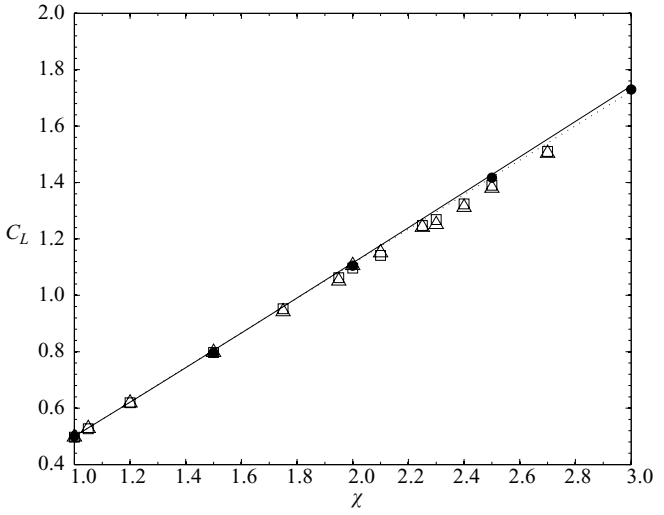

FIGURE 7. Lift coefficient for $Re = 4000$. □ $Sr = 0.02$ and △ $Sr = 0.2$. ●: theoretical prediction by Naciri (1992); dotted line: relation (4.1); solid line: added mass coefficient $C_M(\chi)$.

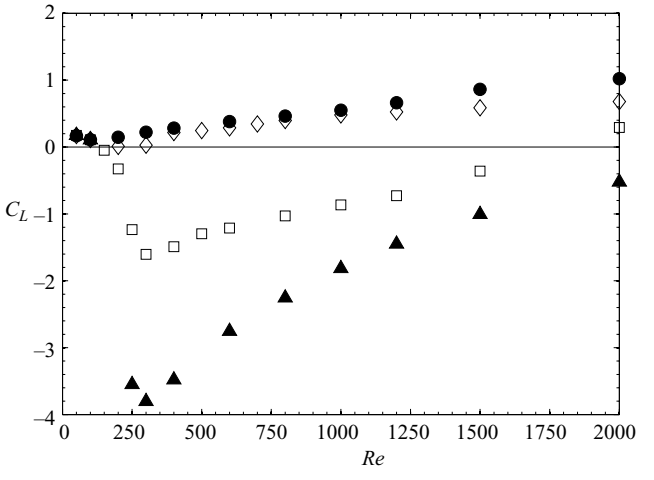

FIGURE 8. Lift coefficient C_L versus the Reynolds number Re for $\chi = 2.5$ and: ▲ $Sr = 0.008$, □ $Sr = 0.02$, ◆ $Sr = 0.1$, ● $Sr = 0.2$.

of figure 5 (i.e. for $\chi < \chi_0(Sr)$) or in the high-Re regime displayed in figure 7. This sensitivity to Sr is emphasized in figure 8 which shows how the evolution of C_L with Re is affected by the shear rate for a given bubble geometry ($\chi = 2.5$). In particular, this figure reveals that the lift force does not reverse whatever Re for the highest two shear rates $Sr = 0.1$ and $Sr = 0.2$. Actually, this was found to be true throughout the whole range of χ we explored. In contrast, C_L becomes negative beyond $Re \approx 150$ for the lowest two values of Sr. In this case, the minimum of C_L is reached for $Re \approx 300$ for both values of Sr. Quite surprisingly at first glance, the magnitude of this minimum is found to increase strongly when Sr decreases. As mentioned above, there is a subregion within which the lift force exhibits periodic oscillations about the mean negative value reported in the figure. For instance, the lift coefficient computed

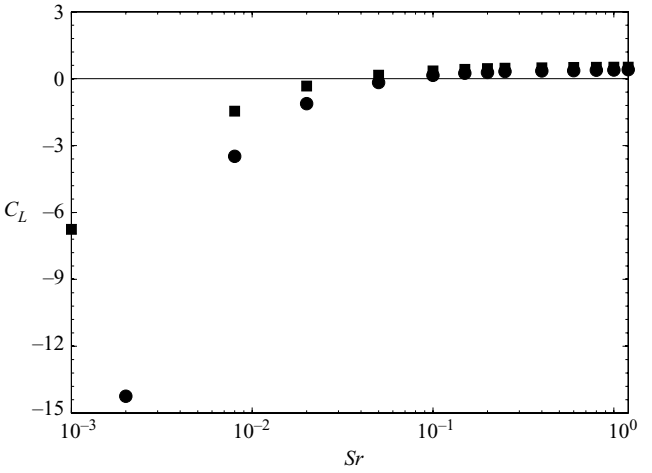

FIGURE 9. Lift coefficient C_L versus the relative shear rate Sr for $Re = 400$ and: ■ $\chi = 2.25$, ● $\chi = 2.5$.

in the case $\chi = 2.5$, $Re = 400$, $Sr = 0.008$ oscillates between -2.5 and -4.5 with a reduced frequency $fb/U_0 \approx 0.17$.

The variations of C_L with Sr at low shear rate may be better appreciated in figure 9 where we plotted the evolution of the lift coefficient up to $Sr = 1$ for a given Reynolds number and two bubble geometries. This figure confirms that C_L is almost independent of Sr when the lift force is positive (here for $Sr \geqslant 0.05$, approximately). In contrast, a dramatic variation of C_L with Sr is observed in the region where the lift force is negative. A detailed examination reveals that C_L varies essentially as Sr^{-1} in this regime. Turning back to the definition of C_L (see § 2), this behaviour obviously means that the lift force has become almost independent of the shear rate, making the scaling we adopted for this force, and hence the definition of the lift coefficient, inappropriate in this regime.

The influence of the relative shear rate on the reversal of the lift force is finally summarized in figure 10 which shows the sign of C_L in the (χ, Sr) phase plane for a fixed Reynolds number, namely $Re = 400$. At this specific Re, we see that C_L does not change sign whatever $\chi < 2.7$ for $Sr > 0.07$. For lower shear rates, a finite value of the critical aspect ratio $\chi_0(Sr)$ is found to exist, which quickly decreases as Sr decreases until it becomes almost independent of the shear rate for $Sr \leqslant 0.04$.

4.2. *Torque*

To complete this description of global dynamic quantities, let us briefly describe the results concerning the torque acting on the bubble. Indeed, unlike a spherical bubble, an oblate bubble experiences a non-zero torque when moving in a linear shear flow. More precisely, all contributions to the surface stress are locally normal to the surface in both cases (owing to the shear-free condition) so that a departure from the spherical shape is required for the torque to be non-zero. We extended Naciri's theory to determine the torque experienced by an oblate bubble set fixed in a weak inviscid linear shear flow (Adoua 2007). The result was obtained in the form of an integral which was evaluated numerically. For $\chi \leqslant 3$, the final result can be fitted with an accuracy better than 1 % through the simple relation

$$C_{\Gamma\infty} = -0.27(\chi - 1)^{0.7}. \tag{4.3}$$

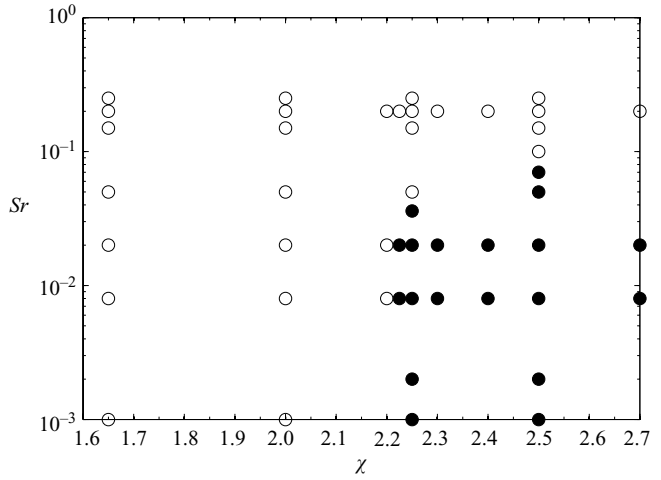

FIGURE 10. Phase diagram (χ, Sr) showing the sign of the lift force for $Re = 400$. ○ $C_L > 0$, ● $C_L < 0$.

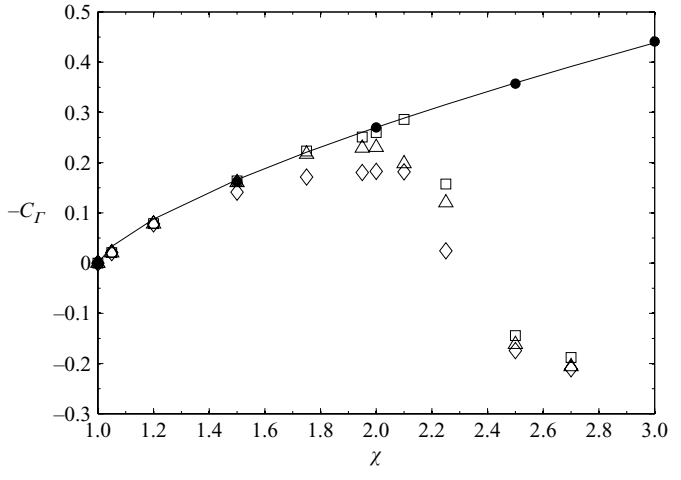

FIGURE 11. Evolution of $-C_\Gamma$ with χ for $Sr = 0.02$. ● analytical solution; — relation (4.3); numerical simulations: ◇ $Re = 400$, △ $Re = 1000$, □ $Re = 1500$.

Obviously the predicted torque is negative, corresponding to a rotation imposed by the upstream vorticity $\boldsymbol{\omega}_\infty = -\alpha \boldsymbol{e}_z$.

The computed variations of the dimensionless torque C_Γ with the aspect ratio and the Reynolds number are shown in figure 11 for $Sr = 0.02$. In line with the results we obtained for the lift force, the evolution of C_Γ exhibits two markedly different regimes, depending on the aspect ratio. For $\chi \leqslant \chi_0(0.02) \approx 2.2$, the torque increases monotonically with the aspect ratio and follows the general evolution predicted by the analytical solution, the difference $C_\Gamma - C_{\Gamma\infty}$ decreasing as $\chi - \chi_0$ increases. In contrast, for $\chi \geqslant \chi_0(0.02)$, the torque starts decreasing sharply with χ and eventually reverses for all Reynolds numbers we computed. Under such conditions, the bubble tends to rotate in a direction opposite to that imposed by the upstream vorticity. For

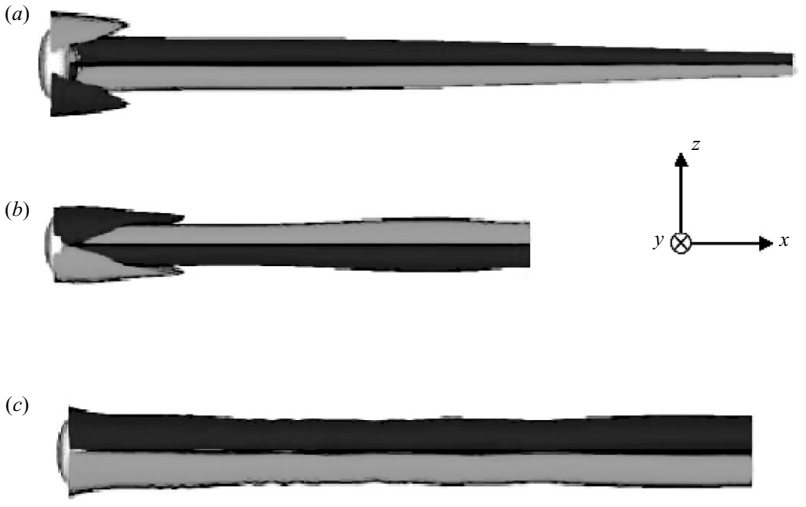

FIGURE 12. Typical isocontours of the normalized trailing vorticity $\omega_x b/U_0$ in the (x, z)-plane for $\chi = 2.25$ and $Sr = 0.02$. (*a*) $Re = 200$ ($C_L \approx 0.22$), (*b*) $Re = 400$ ($C_L \approx -0.33$), (*c*) $Re = 1000$ ($C_L \approx 0.41$). The trailing vorticity is <0 within the darkest thread.

the highest aspect ratios we considered, say $\chi \geqslant 2.5$, the values of the torque coefficient exhibit some sort of convergence towards $C_\Gamma \approx -0.20$ throughout the whole range of Re. The phase diagram displaying the sign of the torque in the (χ, Re) plane (not shown) is almost identical to that of figure 6, strongly suggesting that the reversal of the lift force and that of the torque are two manifestations of the same physical mechanism.

5. Discussion

5.1. *The two mechanisms of streamwise vorticity generation*

As is well established at least since Lighthill's landmark work (Lighthill 1956), the lift force on a non-lifting body of finite span is a direct consequence of the presence of a pair of counter-rotating streamwise vortices in its wake. Hence the key of the observed lift reversal has to be seeked in the mechanisms capable of generating such streamwise vortices. Figure 12 displays the isosurfaces of the trailing vorticity ω_x for a given χ and Sr and for three different Reynolds numbers. Indeed this vorticity component is organized in two counter-rotating tubes exhibiting mirror symmetry with respect to the (x, y) plane, which is of course the symmetry plane of the undisturbed shear flow. In line with the wake/lift force connection mentioned above, figure 12 shows that the sign of the trailing vorticity in a given thread and that of the lift force follow each other. In particular, this sign is observed to have reversed in figure 12(*b*) ($Re = 400$) which, according to figures 5 and 6, corresponds to a set of parameters for which the lift force is negative.

To better understand the change of sign of the trailing vorticity ω_x, let us consider the Helmholtz equation governing this vorticity component. Neglecting viscous effects, we may write,

$$\left(\frac{D}{Dt} - \frac{\partial U_x}{\partial x}\right)\omega_x = (\boldsymbol{\omega}\cdot\nabla)_{cs} U_x, \tag{5.1}$$

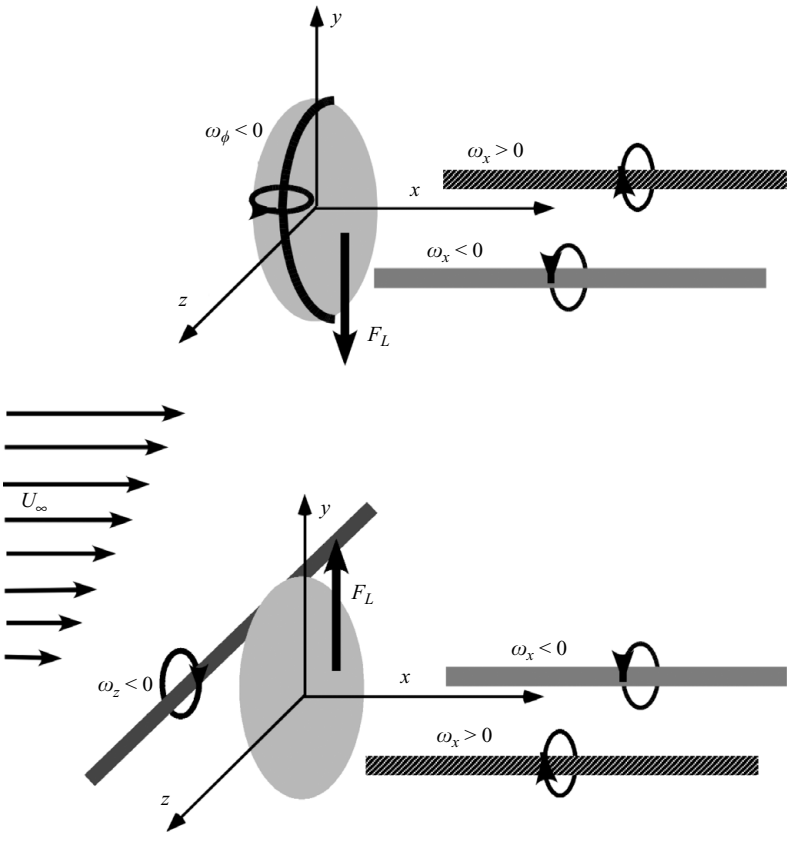

FIGURE 13. Sketch of the two mechanisms responsible for the lift force. Top: the '*S*' mechanism due to the surface vorticity induced by the shear-free condition; bottom: the '*L*' mechanism associated with the upstream vorticity.

where $D/Dt = \partial/\partial t + \boldsymbol{U}\cdot\nabla$ is the material derivative and $(\boldsymbol{\omega}\cdot\nabla)_{cs}U_x$ denotes the contribution to the stretching/tilting term due to vorticity components lying in planes perpendicular to the upstream flow. As the trailing vorticity is zero, far upstream of the bubble, its generation is entirely due to the latter contribution. Ahead of the bubble, the vorticity is $\boldsymbol{\omega}_\infty = -\alpha\boldsymbol{e}_z$, so that $(\boldsymbol{\omega}\cdot\nabla)_{cs}U_x \approx -\alpha\partial U_x/\partial z$. For $z>0$ (resp. $z<0$), $\partial U_x/\partial z$ is >0 (resp. <0) because fluid particles have to accelerate to go around the bubble (see figure 12). Therefore, $(\boldsymbol{\omega}\cdot\nabla)_{cs}U_x$ is <0 for $z>0$ (resp. >0 for $z<0$). This is the classical Lighthill mechanism (Lighthill 1956; Auton 1987) (hereinafter referred to as the '*L*' mechanism) which corresponds to a lift force directed towards positive y (figure 13, bottom).

Let us now consider the contribution to the stretching/tilting term $(\boldsymbol{\omega}\cdot\nabla)_{cs}U_x$ of the vorticity $\boldsymbol{\omega}_s$ produced at the bubble surface. If the upstream flow is uniform, the shear-free condition is known to generate a non-zero azimuthal vorticity component. Therefore, in a cylindrical coordinate system (r,ϕ,x), the bubble surface $r=r_0(x)$ may be considered as a vortex sheet with $\boldsymbol{\omega}_s = \omega_\phi(x)\boldsymbol{e}_\phi$. When the upstream vorticity $\boldsymbol{\omega}_\infty$ is non-zero, the above picture still holds approximately, provided the strength of $\boldsymbol{\omega}_s$ is much larger than that of $\boldsymbol{\omega}_\infty$. The latter condition is always satisfied here because the surface vorticity (normalized by b/U_∞) is known to be of $O(\chi^3)$ for large enough Reynolds number and aspect ratio (Magnaudet & Mougin 2007), while the

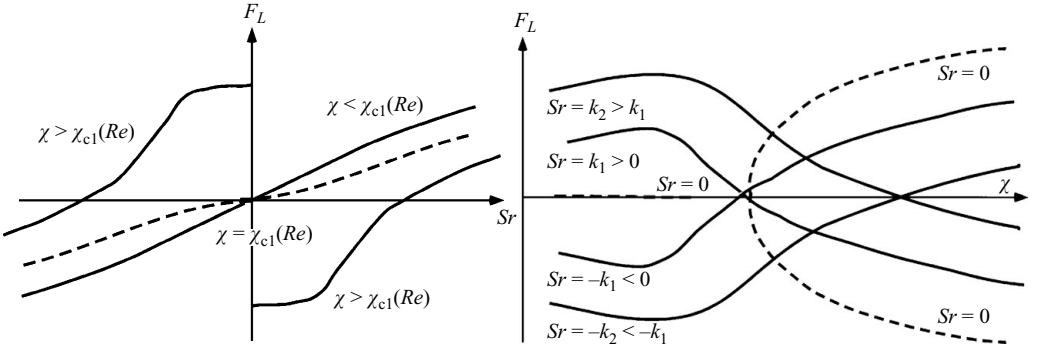

FIGURE 14. Schematic evolution of the lift force with the aspect ratio χ and the relative shear rate Sr for a fixed, slightly supercritical Reynolds number $Re > Re_{c1}(\chi)$.

normalized upstream vorticity is of $O(Sr)$. This surface vorticity obviously results in a contribution $\boldsymbol{\omega}_s \cdot \nabla U_x$ to the stretching/tilting term. As the potential flow around the bubble is such that $\partial U_x/\partial r < 0$ for $r = r_0(x)$, the surface vorticity must balance the corresponding velocity gradient at the surface for the shear-free condition to be satisfied. Therefore $\boldsymbol{\omega}_s$ is negative since it corresponds to an increase of the streamwise velocity towards the flow interior. For $z > 0$ (resp. $z < 0$), the direction of the upstream velocity gradient imposes $\nabla_\phi U_x < 0$ (resp. > 0) (see figure 1), making the contribution of $\boldsymbol{\omega}_s$ to $(\boldsymbol{\omega} \cdot \nabla)_{cs} U_x$ positive for $z > 0$ and *vice versa* (see figure 13, top). In what follows, this mechanism associated with vorticity generation at the bubble surface will be referred to as the '*S*' mechanism.

The above analysis makes it clear that the respective contributions to the trailing vorticity generation of the surface vorticity $\boldsymbol{\omega}_s$ and of the upstream vorticity $\boldsymbol{\omega}_\infty$ have opposite signs. Then, based on (5.1), it could be tempting to seek an estimate of the associated two contributions to the stretching/tilting term in terms of χ and Sr, so as to derive a criterion aimed at predicting under which conditions the *S* mechanism may become dominant. It is easy to see that such an attempt would necessarily be unsuccessful. For instance, it would fail to explain why the generation of the lift force is dominated by the *L* mechanism whatever χ and Sr when the Reynolds number is large enough, or why the *S* mechanism has little influence on the lift force whatever Sr for $\chi < 2.0$. The reason, as will become clear in the next subsection, is that the entire picture is dominated by finite-Reynolds-number effects which, under certain conditions, result in an instability of the bubble wake.

5.2. *Connection with wake instability in an unsheared flow*

Wake instability of an oblate bubble held fixed in a uniform flow was studied in detail using DNS by Magnaudet & Mougin (2007). This study revealed that the axisymmetric wake is stable whatever be the Reynolds number for bubbles with an aspect ratio χ less than the critical value $\chi_{c0} = 2.21$. Beyond this point, there is a finite range of Reynolds number $[Re_{c1}(\chi), Re_{c2}(\chi)]$ within which the wake is fully three-dimensional and yields a non-zero lift force (for $\chi \leqslant 2.5$, this range corresponds to the domain limited by the solid curve in figure 6). In particular, the wake loses its axisymmetry for $Re = Re_{c1}(\chi)$ through a stationary supercritical bifurcation leading to a steady wake made of two counter-rotating streamwise vortices. As the Reynolds number still increases beyond $Re_{c1}(\chi)$, the three-dimensional wake undergoes a series of bifurcations, beginning with a secondary supercritical Hopf bifurcation leading to a periodic vortex shedding regime. In this unsheared situation, the vorticity produced

at the surface of the bubble by the shear-free condition is entirely responsible for the generation of the lift force. Since the base flow exhibits a rotational symmetry about the symmetry axis, the vorticity sign in each vortex is dictated by the initial disturbance required to break the symmetry of the system.

The reason why the wake is unstable only within a finite range of Reynolds number may be readily understood by examining how the surface vorticity $\boldsymbol{\omega}_s$ and the surface vorticity flux $\nu\partial\boldsymbol{\omega}_s/\partial n$ ($\partial/\partial n$ denoting the normal derivative at the bubble surface) evolve with Re for a given bubble shape. As reminded above, for large enough Re, the former quantity is of $O(\chi^3)$ once normalized by b/U_∞. Combining this result with the scaling of the surface boundary layer thickness, namely $b\chi^{-1}Re^{-1/2}$ (Magnaudet & Mougin 2007), the surface vorticity flux is found to be of $O(\chi^4 Re^{-1/2})$ once normalized by U_∞^2/b. Therefore, the amount of vorticity that enters the flow through the bubble surface tends to zero as Re becomes very large. Its χ^4-dependency makes it grow rapidly with the bubble aspect ratio and this growth may balance the $Re^{-1/2}$ decay at moderate to large Re, resulting in an $O(1)$ surface vorticity flux responsible for the wake instability. However, this decay eventually dominates and allows the wake to recover its stability beyond the critical Reynolds number $Re = Re_{c2}(\chi)$. Note that the picture is completely different in the case of a solid body for which the surface vorticity flux is of $O(1)$ whatever be Re, owing to the $O(Re^{1/2})$ growth of the surface vorticity with the Reynolds number.

When a weak shear is present in the upstream flow ($Sr \ll 1$), the wake structure behind a bubble with $\chi > \chi_{c0}$ and $Re_{c1}(\chi) < Re < Re_{c2}(\chi)$ is essentially driven by the same instability mechanism. However, the upstream shear $\nabla_\phi U_x$ now provides the outer disturbance that selects the sign of the streamwise vorticity in the wake in a deterministic manner. Therefore, in line with the above discussion, one expects the sign of the lift force associated with a given sign of α in this regime to be opposite to that which would result from the L mechanism. This is exactly what is observed in figure 6. Also, as the negative lift force for such small Sr is almost entirely due to the above wake instability mechanism and not to the shear, it scales with ρU_0^2, and not with $\rho\alpha U_0$ as initially postulated in the definition of the lift coefficient. Hence this scenario explains why in the left part of figure 9 corresponding to small shears, C_L is observed to be proportional to Sr^{-1}. Then, as Sr increases, so do the effects of the L mechanism, while the vorticity production at the bubble surface and hence the associated streamwise vorticity production is essentially unchanged. This is why in the (χ, Re) plane the size of the domain within which the effect of the S mechanism is dominant decreases. Finally, when the shear rate exceeds a critical value $Sr_c(\chi, Re)$, effects of the L mechanism become dominant, making the lift force recover its usual sign, as observed in figure 10.

Returning momentarily to figure 6, we note that the lower critical Reynolds number in presence of a weak shear, $Re_1(\chi, Sr)$, and the corresponding critical aspect ratio, $\chi_1(Sr, Re)$, are slightly lower than their respective counterparts in the unsheared situation, $Re_{c1}(\chi)$ and $\chi_{c1}(Re)$ (see the black symbols just below the lower branch of the solid line). This suggests that wake destabilization is favoured by shear, as in the case of a solid sphere (Sakamoto & Haniu 1995). In contrast, as $\chi - \chi_0$ increases, the upper Reynolds number bounding the domain where the lift force is negative, $Re_2(\chi, Sr)$, becomes significantly lower than its unsheared counterpart $Re_{c2}(\chi)$. This is because in this high-Re range, the negative lift force in the absence of shear decreases as Re increases, since the wake is progressively recovering its stability, making the corresponding time-averaged lift coefficient be a decreasing function of $Re - Re_{c1}(\chi)$ (Magnaudet & Mougin 2007). Hence this residual negative contribution

may be cancelled well below $Re_{c2}(\chi)$ by the positive contribution provided by the L mechanism which is virtually independent of Re in this regime.

The general evolution of the lift force F_L we just described is schematically depicted in figure 14 which presents cross-sections of the phase space (χ, Sr, Re) at a given Reynolds number Re slightly larger than the critical value $Re_{c1}(\chi)$. At this particular Reynolds number and for a vanishingly small shear rate, the sign of the lift force reverses when χ exceeds $\chi_{c1}(Re)$ (obviously $\chi_{c1}(Re) \geqslant \chi_c$). Then for $\chi < \chi_{c1}(Re)$, F_L results essentially from the L mechanism, so that its sign directly follows that of the shear rate (figure 14 left). In particular, $F_L = 0$ for $Sr = 0$. In contrast, for $\chi > \chi_{c1}(Re)$, F_L and Sr have opposite signs for small enough shear rates and there is a discontinuity of F_L for $Sr = 0$, corresponding to the fact that the non-zero lift force generated by the wake instability changes sign when Sr goes from 0^- to 0^+. The lift force is almost independent of Sr for such low shear rates. Then, as Sr increases for a given supercritical χ, the magnitude of this 'inversed' lift force decreases, until F_L recovers the sign of Sr when the effect of the L mechanism becomes large enough. Conversely, for a given shear rate (figure 14, right), F_L first increases with the aspect ratio for $\chi < \chi_{c1}(Re)$, in accordance with the inviscid prediction. Then, for $\chi \approx \chi_{c1}(Re)$ and for small enough shear rates, the magnitude of F_L decreases sharply because effects of the L and S mechanisms become of comparable magnitude. For each value of Sr, there is a critical value $\chi_1(Sr, Re)$ (with $\chi_1(Sr, Re)$ slightly smaller than $\chi_{c1}(Re)$ for small but finite Sr owing to the reason mentioned above) at which the lift force vanishes for the Reynolds number under consideration; then the larger Sr, the larger $\chi_1(Sr, Re)$. Beyond this critical aspect ratio, the lift force reverses, being dominated by the contribution of the S mechanism. Then, the smaller the Sr, the larger the magnitude of the 'inversed' lift force for a given χ.

With the above characteristics of the S mechanism in mind, we can better appreciate the difficulty of building a simple criterion capable of predicting the sign of the lift force. The first problem encountered on this route would be the detailed determination of the region of the phase space (χ, Sr, Re) within which the wake is unstable. In the unsheared case $Sr = 0$, an indirect response was provided by Magnaudet & Mougin (2007) in terms of the maximum vorticity ω_{max} at the bubble surface. They showed that the unstable (χ, Re) region corresponds to that where $\omega_{max} b/U_\infty$ exceeds a critical value that weakly increases with the Reynolds number. Deriving the extension of this instability criterion when $Sr \neq 0$ would require a complete stability study in a three-dimensional phase space. We did not attempt to achieve such an extensive study, owing to the large computational resources it would require. However, would such an instability criterion be available, there would still be a decisive step to achieve before a criterion for lift reversal could be established. The reason is that the magnitude of the lift force due to the S mechanism has to be known to be compared with that due to the L mechanism and this cannot be achieved through simple dimensional arguments. For instance, a naive dimensional estimate would suggest that the stretching/tilting term corresponding to the S mechanism, $\omega_\phi \partial U/r\partial\phi$, is of $O(\chi^3 \alpha U_\infty/b) = O(\chi^3 Sr(U_\infty/b)^2)$ because the external velocity roughly varies by $2\alpha b$ over one bubble diameter. However, this cannot be the case because $\partial U/\partial\phi$ is zero in the base flow in the limit $Sr \to 0$. Hence, in the unsheared case where the latter term is entirely responsible for the streamwise vorticity generation (and thus for the non-zero lift force), this erroneous estimate predicts no streamwise vorticity at all. Similarly, the stretching/tilting term associated with the L mechanism, $\omega_z \partial U/\partial z$, is of $O(\alpha U_\infty/b) = O(Sr(U_\infty/b)^2)$. Hence the above flawed dimensional estimate suggests that the ratio of the S and

L stretching/tilting terms is of $O(\chi^3)$, i.e. it is independent of the shear rate. This is obviously wrong since we know that for a given (χ, Re) the lift force is negative for small shears but recovers its usual sign when Sr is large enough. Based on these remarks, it is clear that the correct order of magnitude of the stretching/tilting term associated with the S mechanism has to be evaluated by considering the magnitude of $\partial U/\partial\phi$ once the wake is unstable, i.e. the magnitude of the velocity gradient of the unstable mode(s) in the azimuthal direction once the instability has saturated. Clearly this quantity evolves as $(\chi-\chi_c)^{1/2}$, $(Re-Re_c)^{1/2}$ and $(Sr-Sr_c)^{1/2}$ close to the threshold (χ_c, Re_c, Sr_c) of the instability (since the latter is supercritical, as shown by Magnaudet & Mougin 2007 in the case $Sr=0$) but its evolution further away from the threshold is unknown. The above two key problems, especially the second one, make the building of a simple criterion capable of predicting the reversal of the lift force a highly non-trivial task.

5.3. *Comparison with previous work*

The clearest experimental evidence for the migration reversal of oblate bubbles in a linear shear flow was reported by Tomiyama *et al.* (2002). These authors released air bubbles into a Couette flow generated by rotating a belt immersed in a tank filled with a mixture of glycerol and water. By varying the composition of this mixture, they were able to record the migration of bubbles in liquids of viscosity ranging from 18 to 90 times that of water. Several experimental limitations and computational over-simplifications prevent a thorough quantitative comparison between these experimental observations and present results. On the experimental side, the most severe of these is that, owing to the polar nature of water, surfactants are certainly present at the bubble surface. Therefore, the shear-free condition at the gas–liquid interface is probably not fully satisfied which, for a given bubble shape, contributes to increasing the vorticity produced at the bubble surface. On the computational side, the assumption of a spheroidal shape with a perfect fore-aft symmetry is only valid at sufficiently high Reynolds numbers. Actually, even for Reynolds numbers of some hundreds, real bubbles have a quite flat front and a rounded rear owing to small viscous effects. Despite these differences, a qualitative comparison can be performed at least with experimental data obtained in the least viscous oil, which corresponds to the situation in which bubbles have the largest Reynolds number and the largest rising speed and hence have accumulated the smallest amount of surfactant at a given altitude in the tank. The corresponding data indicate that, for the weakest shear rate, i.e. $Sr\approx 0.05$, a bubble with an aspect ratio $\chi=2.06$ experiences a small normal migration, whereas another bubble with $\chi=2.46$ exhibits a clear 'anomalous' migration, both of them having a Reynolds number in the range 95–120. A crude interpolation based on the lateral distances travelled by the two bubbles at a given height in the tank suggests that the migration reverses for $\chi\approx 2.22$. This critical aspect ratio is well in the range of χ where present computations predict that the lift force changes sign in a weak shear flow (see figure 6). Nevertheless, a more relevant comparison may be obtained by taking into account the slight fore-aft asymmetry of real bubbles in the way suggested by Zenit & Magnaudet (2008). These authors pointed out that the most relevant geometrical property of a spheroidal bubble with respect to surface vorticity generation is its maximum curvature, reached on the equator. They noticed that given this fore-aft asymmetry, the perfect oblate spheroid that best approaches the maximum curvature of the real bubble has an aspect ratio about 10 % higher than that directly deduced

from the overall bubble shape. Hence the corrected critical aspect ratio that can be inferred from the experiments is about 2.45. On the other hand, the prediction reported in figure 5 indicates that the lift force on a bubble rising at $Re = 100$ reverses for $\chi \approx 2.55$ for a shear rate $Sr = 0.02$. Given the various uncertainties mentioned above, this comparison indicates that the present predictions and the experimental data are in good agreement for this specific set of parameters. It would of course be of great interest to pursue this comparison for higher Reynolds number but the required experimental data do not seem to be available yet.

Let us finally point out that the migration reversal phenomenon was also observed, both experimentally (Tomiyama *et al.* 2002) and computationally (Ervin & Tryggvason 1997; Sankaranarayanan & Sundaresan 2002), in liquids of much higher viscosity. The associated flow conditions correspond to much lower Reynolds numbers (typically $Re = O(10)$) and much higher shear rates (typically $Sr = O(1)$), while the Weber numbers are typically of $O(1)$. For reasons discussed in § 2, the bubble shapes observed in this flow regime are far from oblate spheroids and do not even exhibit axisymmetry because most of the deformation is due to the shear rather than to the slip, as in low-Re flows. For this reason, the physical mechanism that leads to the inversed migration under such conditions has nothing to do with that explored here. Actually, it is known that low-Re buoyant deformable bubbles moving in a shear flow experience a deformation-induced lift force which pushes them towards the high-velocity side of the shear flow (Magnaudet, Takagi & Legendre 2003). This mechanism subsists in the low- to moderate-Re regime and combines with the usual inertial migration mechanism that tends to push bubbles in the opposite direction. Therefore, when the deformation exceeds some threshold, the former effect dominates, leading to the migration reversal observed in the aforementioned experiments and computations.

6. Conclusions

We computed the force and torque experienced by an oblate bubble of prescribed shape held fixed in a linear shear flow in the regime of moderate to high Reynolds numbers and weak relative shear rates. This simplified model is a valid representation of real bubbles rising in low-viscosity liquids for $Re = O(10^2 - 10^3)$, $We = O(1)$ and $Sr \ll 1$. The numerical results confirm a striking behaviour already reported in several laboratory experiments. That is, when the bubble aspect ratio is large enough, the direction of the bubble lateral migration may reverse compared to that observed for a spherical bubble and to that predicted by inviscid theory for any bubble oblateness. A similar reversal was observed for the torque experienced by the bubble. The flow conditions for this lift and torque reversal to occur were clarified in terms of the bubble aspect ratio, rise Reynolds number and dimensionless shear rate. In particular, it was found that the lift reversal may happen only for large enough aspect ratios, typically $\chi > 2.2$, and weak enough shear rates, typically $Sr < 0.1$, the Reynolds number having to be larger than 10^2, approximately (actually the critical shear rate (resp. Reynolds number) increases (resp. decreases) with the bubble oblateness). Few complete experimental data are available in the regime considered in this work but they do support present predictions in terms of both critical aspect ratio and Reynolds number.

Not surprisingly, the analysis of the flow structure revealed that the origin of this force/torque reversal is directly linked to the sign of the trailing vorticity which is concentrated within two counter-rotating threads in the bubble wake. We showed that

the trailing vorticity induced through the usual tilting mechanism by the azimuthal vorticity generated at the bubble surface by the shear-free condition and that resulting from the classical Lighthill mechanism have opposite signs. Therefore, when the streamwise component of the stretching/tilting term is dominated by the vorticity produced right on the bubble, the lift force changes sign. The required conditions for this scenario to occur are of course fulfilled when the bubble wake becomes unstable and the outer shear is weak. Under such conditions, the essential role of the outer shear is to select the sign of the vorticity within each of the two streamwise vortices that set in downstream of the bubble, whereas the strength of the lift force associated with this pair of vortices remains almost independent of this outer shear. This mechanism explains why, for weak enough shears, the range of aspect ratios and Reynolds numbers for which the reversal of the lift force is observed almost coincides with that within which the axisymmetric wake of a bubble embedded in a uniform stream is unstable to infinitesimal disturbances.

REFERENCES

Adoua, S. R. 2007 Hydrodynamique d'une bulle déformée dans un écoulement cisaillé. *Thèse de Doctorat*, Inst. Nat. Polytech. Toulouse (available online at http://ethesis.inp-toulouse.fr/archive/00000458/).

Auton, T. R. 1987 The lift force on a spherical body in rotational flow. *J. Fluid Mech.* **183**, 199–218.

Auton, T. R., Hunt, J. C. R. & Prud'homme, M. 1988 The force exerted on a body in an inviscid unsteady non-uniform rotational flow. *J. Fluid Mech.* **197**, 241–257.

Ervin, E. A. & Tryggvason, G. 1997 The rise of bubbles in a vertical shear flow. *J. Fluids Engng* **119**, 443–449.

Kariyasaki, A. 1987 Behavior of a single gas bubble in a liquid flow with a linear velocity profile. In *Proceedings of ASME-JSME Thermal Engng Joint Conf.*, Honolulu Hawaii, pp. 261–267.

Lamb, H. 1945 *Hydrodynamics*, 6th ed. Cambridge University Press.

Legendre, D. & Magnaudet, J. 1998 The lift force on a spherical bubble in a viscous linear shear flow. *J. Fluid Mech.* **368**, 81–126.

Lighthill, J. 1956 Drift. *J. Fluid Mech.* **1**, 31–53.

Magnaudet, J. & Mougin, G. 2007 Wake instability of a fixed spheroidal bubble. *J. Fluid Mech.* **572**, 311–337.

Magnaudet, J., Takagi, S. & Legendre, D. 2003 Drag, deformation and lateral migration of a buoyant drop moving near a vertical wall. *J. Fluid Mech.* **476**, 115–157.

Miloh, T. 2003 The motion of solids in inviscid uniform vortical fields. *J. Fluid Mech.* **479**, 287–385.

Moore, D. W. 1965 The velocity of rise of distorted gas bubbles in a liquid of small viscosity. *J. Fluid Mech.* **23**, 749–766.

Mougin, G. & Magnaudet, J. 2002 Path instability of a rising bubble. *Phys. Rev. Lett.* **88**, 014502.

Naciri, A. 1992 Contribution à l'étude des forces exercées par un liquide sur une bulle de gaz: portance, masse ajoutée et interactions hydrodynamiques. *Thèse de Doctorat*, Ec. Centrale Lyon, France.

van Nierop, E. A., Luther, S., Bluemink, J. J., Magnaudet, J., Prosperetti, A. & Lohse, D. 2007 Drag and lift forces on bubbles in a rotating flow. *J. Fluid Mech.* **571**, 439–454.

Sakamoto, H. & Haniu, H. 1995 The formation mechanism and shedding frequency of vortices from a sphere in uniform shear flow. *J. Fluid. Mech.* **287**, 151–171.

Sankaranarayanan, K. & Sundaresan, S. 2002 Lift force in bubbly suspensions. *Chem. Engng Sci.* **57**, 3521–3542.

Serizawa, A., Kataoka, I. & Michiyoshi, I. 1975 Turbulence structure of air–water bubbly flow II. Local properties. *Intl J. Multiph. Flow* **2**, 235–246.

Tomiyama, A., Tamai, H., Zun, I. & Hosokawa, S. 2002 Transverse migration of single bubbles in simple shear flows. *Chem. Engng Sci.* **57**, 1849–1859.

Tran-Cong, S., Marié, J. L. & Perkins, R. J. 2008 Bubble migration in a turbulent boundary layer. *Intl J. Multiph. Flow* **34**, 786–807.

Wells, J. C. 1996 A geometrical interpretation of force on a translating body in rotational flow. *Phys. Fluids* **8**, 442.

Zenit, R. & Magnaudet, J. 2008 Path instability of spheroidal rising bubbles: a shape-controlled process. *Phys. Fluids* **20**, 061702.